Structure of Offshore Low-Level Jet Turbulence and Implications to Mesoscale-to-Microscale Coupling

Structure of Offshore Low-Level Jet Turbulence and Implications to Mesoscale-to-Microscale Coupling

Balaji Jayaraman[1], Eliot Quon[2], Jing Li[1] and Tanmoy Chatterjee[1]

[1] GE Research, 1 Research Circle, Niskayuna, NY - 12309 , [2] National Renewable Energy Laboratory, 15013 Denver West Parkway, Golden, CO 80401, USA.

E-mail: balaji.jayaraman@ge.com

Abstract.

This paper explores realistic nonstationary atmospheric boundary layer (ABL) turbulence arising from nonstationarity at the mesoscale, particularly within offshore low-level jets with implications to offshore wind farms, using high-fidelity multiscale large-eddy simulations (LES). To this end, we analyzed the single-point turbulence statistical structure of a North-Atlantic offshore LLJ event simulated using high-resolution LES (AMR-Wind). The nonstationary LLJ is simulated using a mesoscale-to-microscale coupled (MMC) simulation procedure involving data assimilation of mesoscale velocity and temperature data from the Weather Research and Forecasting (WRF) model. Unlike the assimilation of mesoscale velocity data into the LES, the direct assimilation of temperature profiles had a strong impact on turbulence stratification, thereby causing erroneous predictions of turbulence both above and within the jet layer. Various approaches to mitigate this effect have resulted in multiple (four) variants of this MMC strategy. Outcomes from this work clearly show that the turbulence within the low-level jet is a strong function of the MMC approach as the turbulence structure within the low-level jet is dependent on the flux of residual turbulence from outside the jet, which in turn depends on the temperature forcing history. Additionally, the turbulence predicted by all these different methods (as well as the observation data) show similar deviations from equilibrium as evidenced by comparisons with idealized atmospheric turbulence structure obtained using the same numerical method. In general, we observe that the predicted LLJ turbulence tends to differ from canonical ABL turbulence with comparable shear. Particularly, the combination of shear and turbulence observed in such nonstationary low-level turbulence cannot be matched using equilibrium settings and therefore, represents a critical use-case for both testing and leveraging meso–micro coupling strategies.

1. Introduction

The structure of turbulence in the atmospheric boundary layer has often been explored synergistically, using both observations [1] and high-fidelity large-eddy simulations [2]. Multiscale modeling of the atmospheric boundary layer (ABL) using data assimilation of coarse-resolution observations/data [3] to model realistic ABL turbulence is a topic of active investigation (e.g., see alternate forcing strategy in [4]), motivated by applications in wind energy [5, 6], unmanned aviation [7] and scalar dispersion [8] applications. In this work, we study the turbulence generated from an MMC large-eddy simulation (LES) of offshore low-level jets (LLJs) to assess modeling sensitivity on the turbulence structure while characterizing the underlying mechanisms. In particular, we use high-resolution LES with different MMC approaches with the aim of capturing the dynamics and turbulence structure within LLJs in a

manner consistent with observation data. The different MMC approaches represent variants of the profile-based data assimilation originally demonstrated [3] including those developed through the course of this particular collaborative project beween GE-GRC and NREL. We note that even though the concept of profile assimilation (either in the mean or at a given space-time instance) is popular and well-entrenched within the weather modeling community (in the form of nudging techniques), its effectiveness in predicting the resulting turbulence field is not clearly established. This paper represents the first of such investigations into this aspect of MMC meteorological simulations.

In this work, we focus on an LLJ occurrence in the North Atlantic, which is represented using the Weather Research and Forecasting (WRF) model and validated against buoy-mounted lidar data [9]. The mesoscale-to-microscale downscaling leverages the horizontal scale separation between the microscale (below the capping inversion) and mesoscale eddies (above the capping inversion) such that the time-varying mesoscale velocity and temperature profiles constrain the turbulence-resolving microscale LES in the mean. The accuracy of the resolved turbulence will depend on both the fidelity of the mesoscale-to-microscale coupling (MMC) strategy (discussed in Section 2) and the forcing profiles obtained from WRF. The overarching scope of the project is to study the microscale features of the wind-plant operating environment as driven by mesoscale weather and identify/mitigate potential deleterious effects on wind farm performance (see companion paper number 536 for LLJ impacts). In this paper, we focus on assessing aspects of the microscale ABL turbulence generation specific to LLJs, both as a function of the MMC strategy as well as its deviation from canonical equilibrium ABL turbulence [10]. We note that the deviations from equilibrium explored in this work is different in origin from terrain-induced non-equilibrium effects [11]. The rest of the paper is organized as follows. In Section 2, we detail the MMC formulation and strategies. In Section 3, we compare the outcomes of the MMC-LES with observation data, characterise deviations from canonical behavior and understand the mechanistic aspects that give rise to differing predictions using MMC-LES. A brief summary of the key takeaway messages are presented in Section 4.

2. Data Assimilation (DA)-Based Meso–Micro Coupling

2.1. Mathematical Formulation

We apply large-eddy simulation to resolve the most energetic scales of turbulence within an evolving atmospheric boundary layer under low-level jet conditions. Given our focus on a small offshore region, we assume that the simulated flow is horizontally homogeneous. Potential heterogeneity effects are then approximated through nonstationarity of the modeled ABL. Our simulation strategy combines first-principles physics modeling with an engineering approach to deriving source terms. These momentum and temperature sources represent key features of the mesoscale background flow, as described and validated in Ref. [3]. The salient features of our multiscale model is summarized below. The transport equations for momentum and virtual potential temperature are:

$$\frac{\partial \bar{u}_i}{\partial t} + \frac{\partial}{\partial x_j}\left(\bar{u}_i \bar{u}_j\right) + 2\epsilon_{ijk}\Omega_j\left(\bar{u}_k\right) = F_{u_i} - \frac{1}{\rho_0}\frac{\partial \bar{p}}{\partial x_i} - \frac{\partial \tau_{ij}^D}{x_j} + \left(\frac{\bar{\theta} - \theta_0}{\theta_0}\right) g_i, \tag{1a}$$

$$\frac{\partial \bar{\theta}}{\partial t} + \frac{\partial}{\partial x_j}\left(\bar{u}_j \bar{\theta}\right) = F_\theta - \frac{\partial q_j}{\partial x_j}. \tag{1b}$$

ρ is a constant density, u_i is the velocity vector, p is the pressure, and θ is the virtual potential temperature; overbars indicate resolved-scale quantities while subscript zeroes indicate reference quantities. The final term in the incompressible Navier-Stokes equations Equation (1a) invokes the Boussinesq aproximation for buoyancy. Other quantities include: ϵ_{ijk} is the alternating tensor , Ω_j is the rotation-rate vector describing the Earth reference frame, g_i is the acceleration

vector, τ_{ij}^D is the modeled deviatoric part of the subgrid-scale stress tensor, and q_j is the modeled subgrid-scale temperature flux vector. F_{u_i} and F_θ are time- and height-varying source terms for momentum and temperature, respectively. They implicitly represent various mesoscale tendencies that contribute to the rates of change of velocity and virtual potential temperature.

In this study, we estimate these tendencies from a mesoscale weather forecasting model and the assimilation is achieved through a proportional controller with a nominal gain (K) of 0.2 s^{-1} (corresponding to a time constant of 5s). Thus, $F_\varphi = K\left(\varphi_{meso} - \langle\bar{\varphi}\rangle\right)$, where F is the source term, φ is the field variable (horizontal velocity components or virtual potential temperature), φ_{meso} is the corresponding mesoscale-specified conditions, and the angle brackets denote planar averaging. In effect, we are nudging the entire microscale simulation domain towards resolved statistical values. Applying F_φ directly in the LES prognostic model strongly enforces the input mesoscale conditions at every time step, but at the cost of potentially disrupting the interdependence between the resolved mean and fluctuating turbulence fields. Consequently, the direct approach yields a forcing that is decoupled at each vertical level. Alternatively, an indirect approach filters F_φ, for example, using a cubic polynomial approximation to bring in some vertical coherence in the forcing source terms. This weak enforcement of the mesoscale tendencies causes the microscale resolved mean turbulence statistics to deviate from the mesoscale profiles while allowing for more organic generation and evolution of the turbulent field.

LES with meso–micro coupling therefore involves modeling decisions, including how to derive the mesoscale tendencies and the approach for coupling to the microscale, i.e., whether to use a direct profile assimilation (DPA) or indirect profile assimilation (IPA) approach, and which approach to apply for which fields. While Ref. [3] considered purely direct and purely indirect profile assimilation, we explore two new hybrid profile assimilation strategies (Table 1). Hybrid I mixes direct and indirect approaches, with DPA of velocity components intending to preserve the accuracy of WRF wind profiles that capture the LLJ of interest, while IPA of temperature allows for flexibility in how the resolved microscale flow modulates the turbulent ABL flow through buoyancy. Hybrid II keeps the IPA temperature forcing in check by applying the indirect temperature forcing of Hybrid I only near the surface within the ABL; the free atmosphere is further assumed to have constant forcing with height. For this study, the vertical gradient of the temperature forcing profile is blended from the local value at 250 m to zero at 350 m above ground level. This additional constraint is consistent with having a height-invariant horizontal temperature gradient aloft: $\frac{d\Theta}{dx} \sim \frac{1}{U_0}\frac{d\Theta}{dt} \sim F_b$, where U_0 is a reference advection velocity and F_b is a baroclinic source term. This simplified representation of baroclinicity, with constant horizontal temperature gradient, is sufficient to show a strong impact on turbulence kinetic energy profiles [12].

The microscale (MMC-LES) model equations ((1a) and (1b)) for this paper are implemented within AMR-Wind, a new, massively parallel tool to model incompressible LES of ABL and designed to run on next-generation computing platforms [13]. This AMR-Wind implementation adopts second order (piecewise parabolic method for the advection) discretizations in space and time. These methods have been validated against reference data from literature [14]. An earlier verion of this implementation was done in NREL's legacy incompressible LES, the Simulator for Wind Farm Applications (SOWFA, [15]). In the subsequent section, we compare outcomes from both these implementations for validation purposes. The subgrid scale parameterization and wall stress model follow the approaches reported in [16] and [10]. The only difference being that the Monin-Obukhov functions used to model the surface stress for stable conditions have been modified as per [17]. A typical set-up of these MMC-LESs is that they are approximated as periodic in the microscale which is acceptable when the mesoscale eddies are much larger than the LES domain of interest and our focus remains on the LES dynamics associated with the passage of the eddy core. The MMC-LES domain size for the LLJ is 5.12km.12km $\times$ 1.28km and discretized uniformly at a resolution of 10 m (33.5M cells).

2.2. Validation Against Observation Data

We study 2020-05-15, a day in which the NYSERDA floating lidar [9] observed an LLJ in the New York Bight that persisted for approximately 9 hours, starting from 15:00 UTC. Selection of this case day was based on the jet-identification criteria of [18] and motivated by the excellent agreement between WRF mesoscale model predictions and the observations. Mesoscale data were provided by the same model setup as used by other researchers that recently studied the same offshore region [19].

Figure 1 illustrates the differences between LES predicted mean fields for the four different MMC approaches, with 10-minute, planar averages plotted. The DPA approach applied to momentum for the "direct" and "hybrid" approaches ensures that the wind fields match the mesoscale solution to within machine precision. In contrast, the IPA approach simulates a sharper, more well-defined nose throughout the simulation and approximately preserves the magnitude, height, and onset time of the jet. Whereas the wind profiles are indistinguishable from the mesoscale input (same as DPA in Figure 1), the momentum forcing profiles (Figure 1, second column) have pronounced differences. The magnitude of the forcing arising from the baseline direct and indirect approaches is relatively low compared to the hybrid approaches, except at the surface; the indirect approach effectively filters out the noise generated by the direct forcing. In contrast, the hybrid approaches have significantly larger forcing magnitudes—this arises from the coupling between momentum and temperature fields through the Boussinesq buoyancy term in Equation (1a). For example, the strong cooling tendency that emerges with "hybrid I" corresponds to the strong momentum forcing (Figure 1, second column–third row). The apparent coupling between the momentum and temperature source terms corresponds to notable differences in the resolved temperature fields (Figure 1, third column). In the same way that the "indirect" approach tends to sharpen the jet nose, it also tends to strengthen the capping inversion, seen as a sharp interface between the boundary layer and free atmosphere (Figure 1, third column). Conversely, "hybrid I" has a deeper boundary layer with a more diffuse interface. The most extreme case is with "hybrid II," in which strong warm-air advection is generated over time by the forcing strategy.

While the flow fields and forcings exhibit large degrees of variability (Figure 2), all approaches agree reasonably with the mean wind speed and direction observed from the buoy lidar. This result is attributed to the accuracy of the WRF prediction. By virtue of the DPA approach for the momentum equation, all of the SOWFA approaches (except "indirect") are indistinguishable in the wind speed and direction plots. Similarly, the two AMR-Wind results are coincident in the figure and indistinguishable. Differences come to light when considering the resolved fluctuations. The direct approach with DPA for temperature generates very little turbulence (blue curve in the lower plot of Figure 2) as the stratification in the raw WRF temperature profiles is too stable and tends to overly suppress the wind shear generated turbulence within the jet. The "indirect" approach allows for deviation from the mesoscale forcing profiles by filtering out the sharp gradients and in the process making the local thermal stratification less stable. At the same time, this approach also modulates the velocity profile within and above the low-level jet, thereby impacting the turbulence generation process. Therefore, even

Table 1. A summary of the forcing strategies applied in this study.

Name	Momentum Assimilation	Virtual Potential Temperature Assimilation
direct	direct (full WRF profile)	direct (full WRF profile)
indirect	indirect (full WRF profile)	indirect (full WRF profile)
hybrid I	direct (full WRF profile)	indirect (full WRF profile)
hybrid II	direct (full WRF profile)	indirect (partial WRF profile)

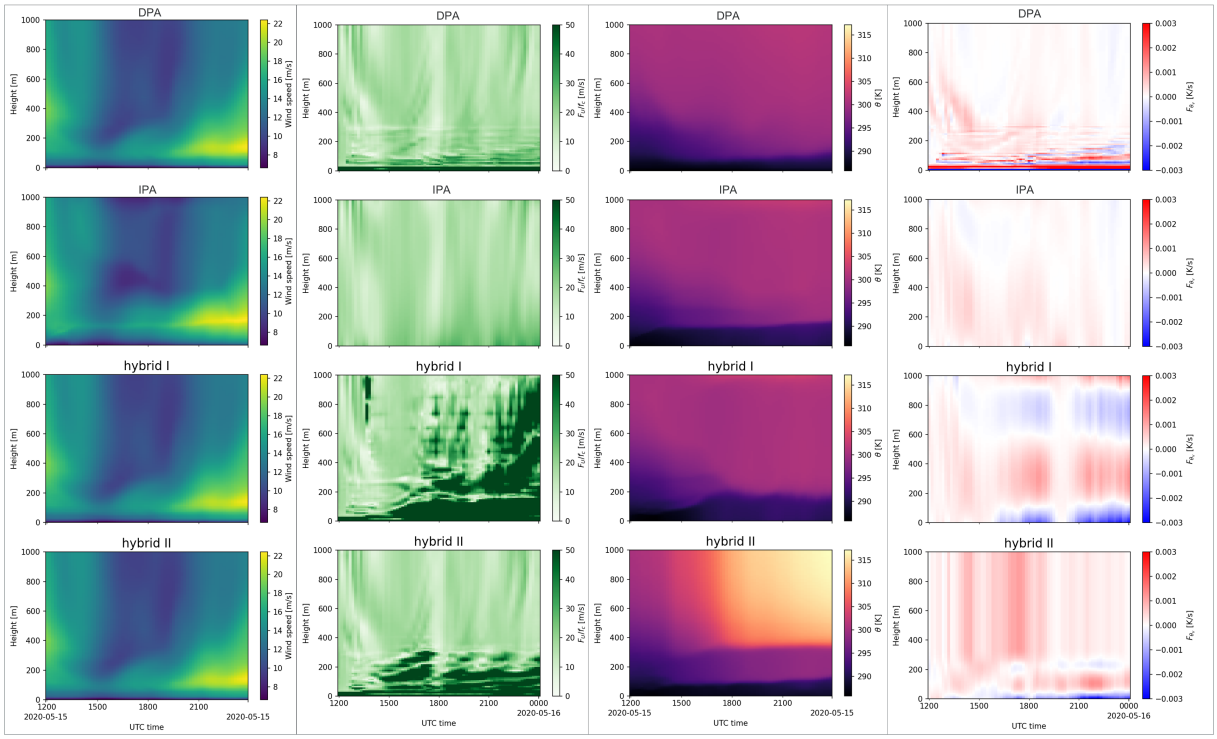

Figure 1. Time–height plots of mean wind speed (first column), wind speed forcing term divided by the Coriolis factor (second column), virtual potential temperature (third column) and virtual potential temperature forcing term (fourth column)

though the resolved turbulence is higher for the indirect MMC approach (orange curve in the lower plot of Figure 2) as compared to the direct approach, it is still an underprediction relative to observational data. The complex forcing behaviors introduced by the hybrid approaches (Figure 1) has the effect of triggering additional turbulence production, as evidenced by the history of turbulence intensity in Figure 2. Lastly, we note that despite differences in initialization time, initial perturbations, and numerical schemes between the two codes, SOWFA and AMR-Wind, show excellent agreement between the hybrid approaches. This confirms that variability in predictions associated with the different MMC strategies are only weakly dependent on the numerical method.

To further assess the validity of these different MMC approaches, we look at profiles of wind speed and wind-speed standard deviation (σ_U, see Figure 3). We note that there is substantial uncertainty in the empirical σ_U correction, calculated onboard the lidar, so we have presented both uncorrected (filled symbols) and corrected (open symbols) values. As with the time histories in Figure 2, the wind profiles show excellent agreement with buoy measurements for the selected time range. In terms of σ_U, the data demonstrate qualitative similarities to a class of LLJ observed onshore under strong wind, weakly stable conditions, categorized as having σ_U attain a maximum aloft [20]. More specifically, this class of LLJ may be described as having a local minima in σ_U at the jet nose, above which σ_U is not constant but increasing. The baseline direct and indirect assimilation results show an approximately monotonic decrease in σ_U with height, consistent with canonical stable boundary layers whereas both the hybrid forcing strategies exhibit the maximum aloft behavior. "hybrid I" has greater resolved turbulence than the other approaches by approximately a factor of two. In comparison, σ_U above and below the jet nose for "hybrid II" is much closer to the experimental value of 0.05 that exhibited similarity across

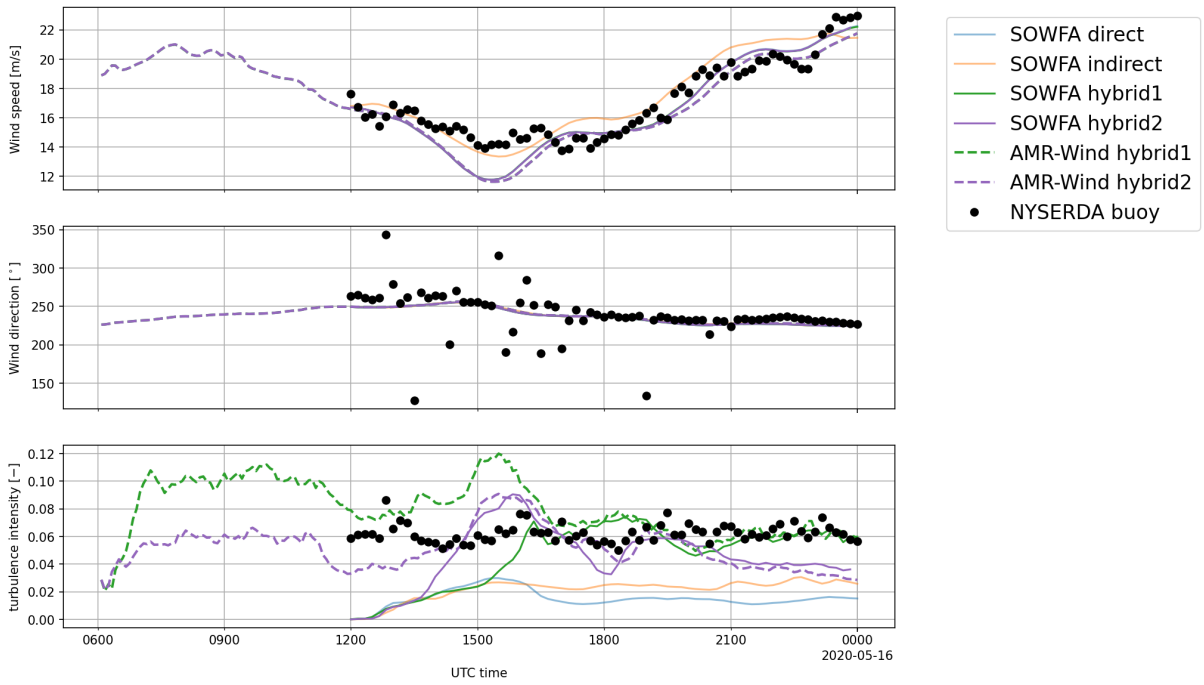

Figure 2. Time history of wind speed, wind direction, and turbulence intensity at 150m above mean sea level, calculated from planar averages

stability conditions and experimental datasets [20].

3. MMC Strategy and LLJ Turbulence Structure

To put these model predictions from the different MMC strategies within the framework of established knowledge from decades of research on canonical ABL turbulence structure, we compare the predicted LLJ turbulence using AMR-wind with corresponding simulations of quasi-equilibrium ABLs over a specified range of stability state parameter, $\zeta = -z_i/L$ and with matching hub height (of a notional wind turbine) wind speed/direction. These LES of canonical ABL at different stability states were executed using the same computational and modeling framework as the MMC simulations, i.e. using the same numerical methods, subgrid and wall stress models. The idealized LES of ABL at different stability stratifications, namely, neutral, unstable (moderately convective) and stable were approximated as horizontally homogeneous by applying periodic boundaries in the horizontal directions. In the vertical direction, a Monin-Obukov similarity based wall stress/heat flux model is provided at the bottom wall for velocity and temperature respectively (see [16] for neutral and unstable and [17] for stable), while free-slip is enforced for velocity and temperature at the top boundary. A domain of size $5.12km \times 5.12km \times 1.28km$ (res. 10m) was adopted for the neutral and unstable states while a smaller domain of $3.2km \times 3.2km \times 0.8km$ (at a finer resolution (res. 6.25m)) was used to simulate the shallow stable boundary layers with smaller horizontal coherence lengths [14]. The different LES were evolved for twelve hours and data for analysis were collected over a subsequent two-hour period. In all, a series of six simulations were carried out - three stable, two unstable and a neutral with global stability parameters, $\zeta = -z_i/L$ of $-0.66, -0.32, -0.08, 0.0, 0.81$ and 3.12, spanning the moderately stable to moderately unstable range. For all these simulations, the ABL height z_i is defined as the maximum value of $d\langle\theta\rangle/dz$ with angle brackets representing the horizontal space-time average over the analysis period. We note that other definitions of z_i

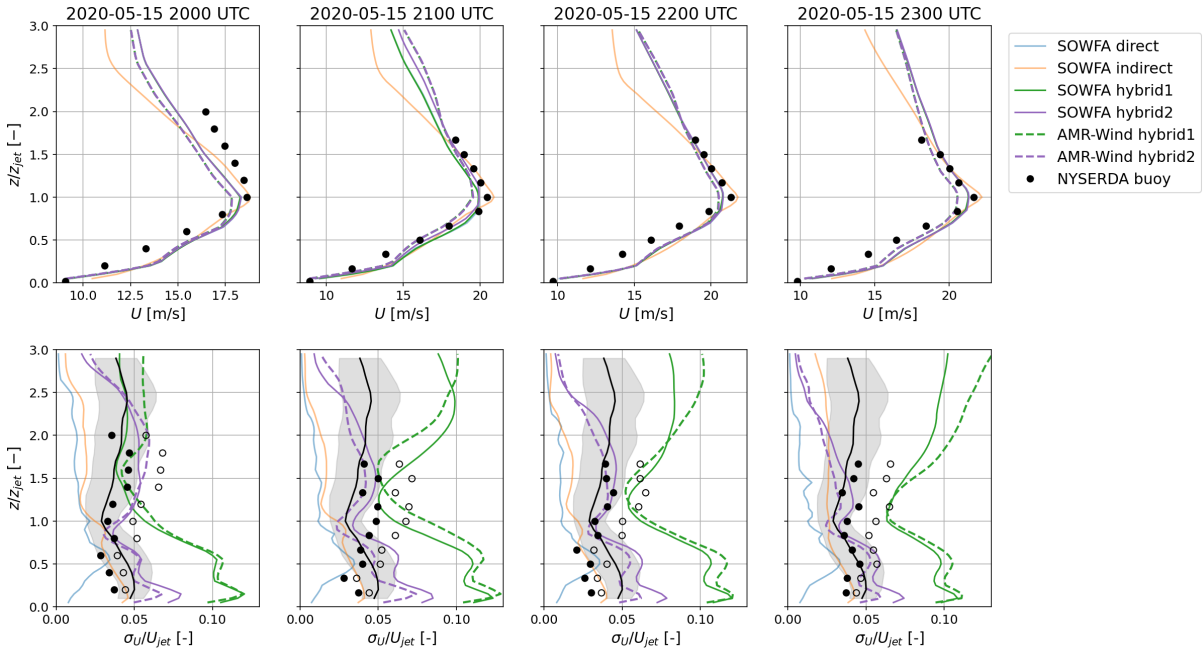

Figure 3. Profiles of wind speed (top row) and wind-speed standard deviation normalized by the instantaneous jet speed, calculated from planar averages; for the latter, reference data are provided in uncorrected (filled symbols) and corrected form (open symbols); the shaded region represents reference data digitized from [20]; for both quantities, the height axis has been normalized by the instantaneous jet height.

generated nearly comparable estimates of the ABL height.

Figure 4 compares the velocity components and the corresponding vertical shear for the different canonical ABL and the MMC-LES of LLJs using "hybrid I" and "hybrid II" approaches. These profiles represent planar-averaged LES data over a relatively stationary 120 minute period from 2100 UTC – 2300 UTC on the day of interest (2020-05-15, Figure 2) for the LLJs. The quasi-equilibrium turbulence profiles are obtained from canonical ABL simulations with constant mesoscale wind such that the hub-height (150 m for the IEA 15MW turbine) wind speed matching that of the LLJ and surface flux values corresponding to $\zeta = -z_i/L \sim -1.0$ to 3.1. We clearly observe that the "direct" forcing of momentum ensures identical velocity profiles for the different MMC approaches while showcasing the peak LLJ shear around the jet nose height of 100 m.

In Figure 5, we compare the LLJ turbulence profiles averaged over the same period as above and compare with the corresponding quasi-equilibrium turbulence structure. The MMC-LES of the LLJ using "hybrid I" (see Table 1) generates turbulence magnitudes that are nearly twice as large as the corresponding magnitudes for idealized ABL across the stable/neutral stability regime and also larger than the moderately unstable case corresponding to $\zeta = 3.1$, observations that are are consistent with Figure 3. However, the "hybrid II" approach with baroclinic forcing above the inversion layer generates turbulence intensities and Reynolds stresses that are more in line with canonical near-neutral and stable ABL estimates.

It is well known that the different canonical ABL states characterize differing levels of vertical mixing from buoyancy relative to shear-induced turbulence where mixing is more diffusive in nature. This mixing in turn can impact the mean velocity profiles, thereby representing the interaction between momentum and buoyancy effects within the boundary layer. Consequently,

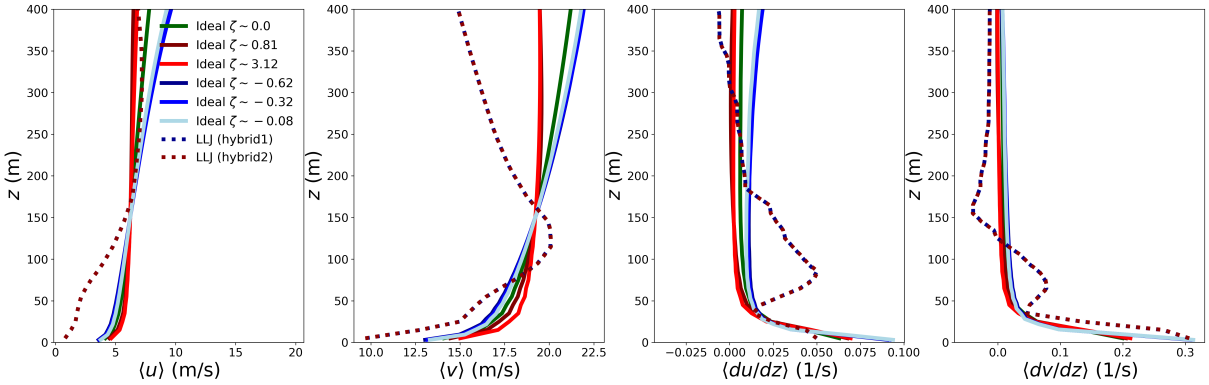

Figure 4. Profiles of the horizontal components and their vertical gradients compared between canonical ABL turbulence at different values of the stability parameter, $\zeta = -z_i/L$ (solid lines) and the LLJ using the different MMC-LES strategies (dashed lines).

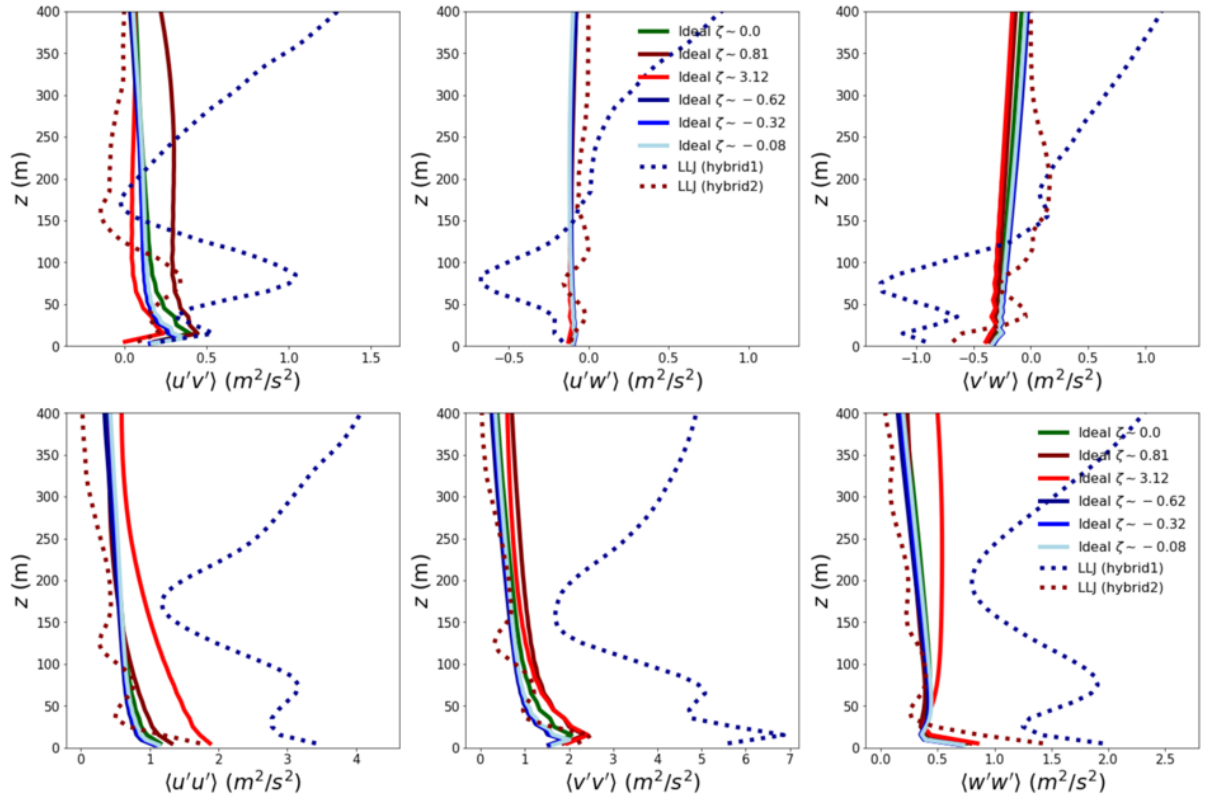

Figure 5. Profiles of the six Reynolds stress components compared between canonical ABL turbulence at different values of the stability parameter, $\zeta = -z_i/L$ (solid lines) and the LLJ using different MMC-LES strategies (dashed lines).

the different turbulence regimes in the ABL are characterized by combinations of shear and turbulence intensity which can be represented using a scatter plot of turbulence intensity (TI) and the shear exponent (α). We explore the use of such a plot to not only characterize the unique combinations of TI–shear that represent the LLJ turbulence, but also the interplay between momentum and buoyancy effects that underpin the outcome of the hybrid MMC-LES

approaches. We show in Figure 6, the plot of TI and α, at a height of 80 m above the ground for the different canonical ABLs as well as the different MMC-LES of LLJ using the two different hybrid methods. To provide additional context, we also include the buoy data. Here, we define TI as $\sqrt{2k/3}/M$ where k is the turbulent kinetic energy, M is horizontal wind speed magnitude at the vertical plane of interest. The shear exponent is defined by, $\alpha_{lo} = log(u_2/u_1)/log(z_2/z_1)$ with subscripts representing vertical measurement locations around the lo level below the jet nose (i.e., $z_{lo} = 80$m). In order to highlight the local stability at the measurement data point, each symbol is colored by an estimate of the local Richardson number.

Figure 6 clearly shows that the turbulence–shear combinations (solid circles) from the canonical states occupy the region close to the axes, with the stable states revealing a high shear–low TI combination while the unstable states are characterized by low shear–high TI. Additionally, all the data from the canonical ABL are neatly clustered by Richardson number, indicating stability as a defining parameter to characterize these states. On the other hand, the simulated LLJ data from the MMC-LES using "hybrid I" approach shows nearly consistent, but higher TI (as compared to canonical stable ABL) over a whole range of shear values and Richardson numbers spanning the near-neutral to stable regime. The lidar observation data from the buoy also show higher turbulence than the canonical stable ABL data but lower than "hybrid I". The "hybrid II" approach is more closer to the canonical data and smaller than the observations — indicative of strong sensitivity from the MMC model. Additionally the LLJ data from simulation and observations show that the clustering of the points around Richardson number is lost unlike that observed for the canonical ABL, indicative of the existence of other scaling dependencies beyond the local Richardson number. These observations suggest that the larger TI within the LLJ is not unique to any particular MMC strategy and qualitatively represents the lidar observation data at the site. We speculate that this *deviation from canonical equilibrium* may be tied to the pervasive nonstationarity that drives diurnal variations and LLJs within atmospheric boundary layers.

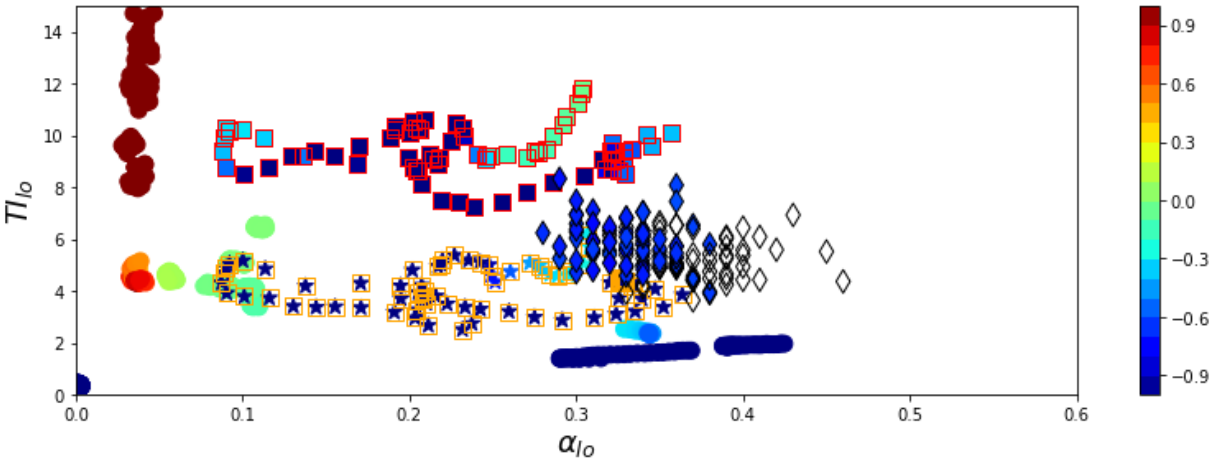

Figure 6. Plot of shear exponent versus turbulence intensity colored by bulk Richardson number at a location of 80m above the surface and below the LLJ nose. Shown are comparisons of data from LES of canonical ABL (circles), "hybrid I" MMC-LES of LLJ turbulence (squares), "hybrid II" MMC-LES of LLJ turbulence (stars) and buoy-mounted lidar data (diamonds).

To understand the larger turbulence predictions within the LLJ using the "hybrid I" MMC approach, we look into the turbulence production metrics for the different methods as well as for the different canonical ABLs. In Figure 7, we look at the shear production of the horizontal turbulence (that is, $\langle u'u' \rangle$ and $\langle v'v' \rangle$) as denoted by $P_{uu}^{sh} = -2\langle u'w' \rangle d\langle u \rangle / dz$ and

$P_{vv}^{sh} = -2\langle v'w'\rangle d\langle v\rangle/dz$ respectively. Note that there is no direct buoyancy production of these horizontal component variances although some of $\langle w'w'\rangle$ may be redistributed into $\langle u'u'\rangle$ and $\langle v'v'\rangle$ through the pressure-strain mechanism. These plots show that the production of both $\langle u'u'\rangle$ and $\langle v'v'\rangle$ are larger for the LLJ as compared to the range of canonical ABL considered and in particular for the LLJ using "hybrid I" MMC approach (as compared to that using "hybrid II" MMC approach). The shear production of turbulence in a horizontally homogeneous setting is given by the product of the appropriate Reynolds stresses, $\langle u'w'\rangle$ and $\langle v'w'\rangle$ and the corresponding vertical mean shear, $d\langle u\rangle/dz$ and $d\langle v\rangle/dz$ respectively. We know from Figure 4 that the mean shear for the LLJ over the period of analysis are the same for both the "hybrid I" and "hybrid II" approaches. This implies that the differences between these different MMC approaches originate from the differences in Reynolds stresses $\langle u'w'\rangle$ and $\langle v'w'\rangle$. We already know that from Figure 5 that larger values of $\langle u'w'\rangle$ and $\langle v'w'\rangle$ (as is $\langle w'w'\rangle$) is observed for the "hybrid I" MMC approach. In Figure 7, we look at the buoyancy and shear production of the Reynolds stress components, $\langle u'w'\rangle$ and $\langle v'w'\rangle$, denoted by $P_{uw}^{sh} + P_{uw}^{buoy} = -\langle w'w'\rangle d\langle u\rangle/dz + \frac{g}{\theta_0}\langle u'\theta'\rangle$ and $P_{vw}^{sh} + P_{vw}^{buoy} = -\langle w'w'\rangle d\langle v\rangle/dz + \frac{g}{\theta_0}\langle v'\theta'\rangle$. We observe that the "hybrid I" MMC approach shows larger production of Reynolds stresses for in spite of the velocity shear being identical for both the hybrid approaches. Therefore, the difference in production of these stresses should come from the buoyancy destruction or through the vertical variance. In Figure 8, we show the different temperature flux components, $\langle u'\theta'\rangle$, $\langle v'\theta'\rangle$ and $\langle w'\theta'\rangle$ which contribute to buoyancy destruction of $\langle u'w'\rangle$, $\langle v'w'\rangle$ and $\langle w'w'\rangle$ respectively. These plots suggest that the buoyancy destruction of $\langle u'w'\rangle$, $\langle v'w'\rangle$ is comparable in the vicinity of the jet, but the destruction of $\langle w'w'\rangle$ is larger in the "hybrid I" MMC approach. This suggests that the larger values of $\langle w'w'\rangle$ for hybrid I that drives the shear production of $\langle u'w'\rangle$ and $\langle v'w'\rangle$ comes from vertical transport of turbulence and not from production. We see some evidence of this in the larger downward vertical flux of temperature as compared to the "hybrid II" MMC approach — implying stronger downward motions in the former and thereby larger Reynolds stresses resulting in higher streamwise turbulence intensity. This suggests that in simulated LLJs, the turbulence within the jet is impacted by residual thermal fluctuations that exist aloft of the jet. Therefore, the accurate modeling of the LLJ using MMC requires accurate capture of the residual layer turbulence. This in a nutshell highlights the complexity of modeling such nonstationary turbulence events as the residual layer physics strongly depends on the ABL time history over entire diurnal cycles.

4. Conclusions

At its core, this work highlights the challenges of multiscale modeling of turbulence in the atmosphere where idealized behavior is rarely observed. The microscale turbulence within the ABL is driven by terrain and mesoscale weather events along with a strong dependence on the history of turbulent flow field. In particular, we observe from this work that the assimilation of mesoscale profile data into microscale simulations, while natural and well accepted by the meteorological (and the broader fluid dynamics) modeling community, does not guarantee accurate turbulence predictions within the ABL. This motivates the need for the different meso–micro coupling methods assessed in this work. While all the different methods "appear" effective in their own right with reasonable qualitative characteristics, realizing the correct quantitative turbulence predictions is much harder. Specifically, the hybrid methods tend to improve the predictive performance of the indirect and direct forcing methods that underestimate the turbulence intensity, but have large effective mesoscale forcing magnitudes and show significant variability. These model-driven sensitivities can be attributed to turbulence dynamics above the LLJ and in the residual layer where downward fluxes of thermal fluctuations contribute to turbulence generation. In such cases, knowledge of observations is a key component of improving model predictions until more reliable prognostic capabilities can be designed and deployed in

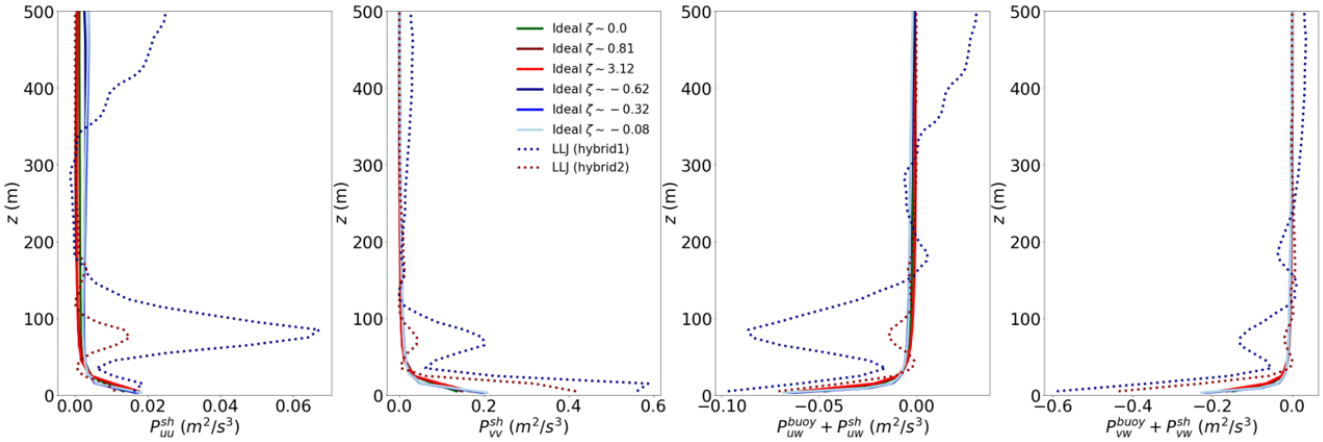

Figure 7. Profiles of the two-hour averaged (2100-2300UTC) production of the horizontal velocity component variances, $\langle u'u' \rangle$ and $\langle v'v' \rangle$, through shear denoted by P_{uu}^{sh} and P_{vv}^{sh}, Reynolds stress $\langle u'w' \rangle$ production through shear and buoyancy, $P_{uw}^{sh} + P_{uw}^{buoy}$ and Reynolds stress $\langle v'w' \rangle$ production through shear and buoyancy, $P_{vw}^{sh} + P_{vw}^{buoy}$. All plots compare data from the different MMC-LES of LLJs (thinner dashed lines) and canonical ABL turbulence (thicker lines).

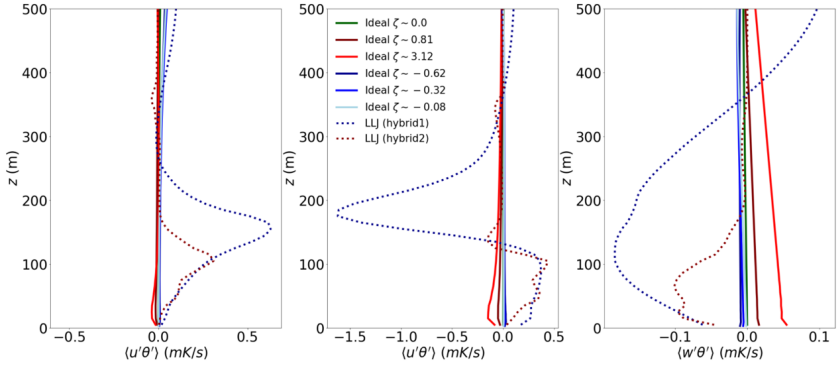

Figure 8. Profiles of the two-hour averaged (2100-2300UTC) temperature fluxes $\langle u'\theta' \rangle$, $\langle v'\theta' \rangle$ and $\langle w'\theta' \rangle$. All plots compare data from the different MMC-LES of LLJs (thinner dashed lines) and canonical ABL turbulence (thicker lines).

the field. At a physical level, we observe that the predicted LLJ turbulence tends to differ from canonical ABL turbulence with comparable shear, suggesting that such nonstationary phenomena represent a unique use-case for both testing and leveraging meso–micro coupling strategies.

5. Acknowledgement

This material is based upon work supported by the U.S. Department of Energy's Office of Energy Efficiency and Renewable Energy (EERE) under the Wind Energy Technologies Office Award Number DE-EE0008390 to the New York State Energy Research and Development Authority for establishing the National Offshore Wind Research Consortium. This report was prepared as an account of work sponsored by an agency of the United States Government. Neither the United States Government nor any agency thereof, nor any of their employees, makes any warranty, express or implied, or assumes any legal liability or responsibility for the accuracy, completeness, or usefulness of any information, apparatus, product, or process disclosed, or represents that its use would not infringe privately owned rights. Reference herein

to any specific commercial product, process, or service by trade name, trademark, manufacturer, or otherwise does not necessarily constitute or imply its endorsement, recommendation, or favoring by the United States Government or any agency thereof. The views and opinions of authors expressed herein do not necessarily state or reflect those of the United States Government or any agency thereof.

This work was also authored in part by the National Renewable Energy Laboratory, operated by Alliance for Sustainable Energy, LLC, for the U.S. Department of Energy (DOE) under Contract No. DE-AC36-08GO28308. Funding provided by the National Offshore Wind Research & Development Consortium through a subcontract with General Electric. The views expressed in the article do not necessarily represent the views of the DOE or the U.S. Government. The U.S. Government retains and the publisher, by accepting the article for publication, acknowledges that the U.S. Government retains a nonexclusive, paid-up, irrevocable, worldwide license to publish or reproduce the published from of this work, or allow others to do so, for U.S. Government purposes.

Computational resources were sponsored by the (i) Department of Energy's Office of Energy Efficiency and Renewable Energy and located at the National Renewable Energy Laboratory and (ii) the Oak Ridge Leadership Computing Facility, which is a DOE Office of Science User Facility supported under Contract DE-AC05-00OR22725.

References

[1] Högström U, Hunt J and Smedman A S 2002 *Boundary-Layer Meteorology* **103** 101–124
[2] Jayaraman B and Brasseur J G 2018 *arXiv preprint arXiv:1807.03336*
[3] Allaerts D J N, Quon E, Draxl C and Churchfield M 2020 *Boundary-Layer Meteorology* **176** ISSN 0006-8314
[4] Jayaraman B, Brasseur J, McCandless T and Haupt S 2014 Nonequilibrium behavior of the daytime atmospheric boundary layer, from LES *APS Division of Fluid Dynamics Meeting Abstracts* pp L25–011
[5] Lavely A W, Vijayakumar G, Craven B, Jayaraman B, Paterson E G, Nandi T N and Brasseur J 2014 Towards a blade-resolved hybrid URANS-LES of the nrel 5-mw wind turbine rotor within large eddy simulation of the atmospheric boundary layer *32nd ASME Wind Energy Symposium* p 0869
[6] Vijayakumar G, Brasseur J, Lavely A W, Jayaraman B and Craven B 2016 Interaction of atmospheric turbulence with blade boundary layer dynamics on a 5MW wind turbine using blade-boundary-layer-resolved CFD with hybrid URANS-LES *34th Wind Energy Symposium* p 0521
[7] Davoudi B, Taheri E, Duraisamy K, Jayaraman B and Kolmanovsky I 2020 *AIAA Journal* **58** 1992–2004
[8] Allamraju R, Jayaraman B, Jacob J D, El-Messidi A and Alkadi N 2019 Plume source inversion with mobile UAS sensing for environmental applications *AIAA Scitech 2019 Forum* p 1062
[9] DNV-GL 2020 NYSERDA floating lidar buoy data online URL `https://oswbuoysny.resourcepanorama.dnvgl.com`
[10] Jayaraman B and Brasseur J G 2021 *Journal of Fluid Mechanics* **913**
[11] Khan S and Jayaraman B 2019 *Fluids* **4** 161
[12] Momen M, Bou-Zeid E, Parlange M B and Giometto M 2018 *Journal of the Atmospheric Sciences* **75** 3797–3821 ISSN 0022-4928, 1520-0469
[13] Sprague M A 2021 Exawind: Predictive wind energy simulations Tech. rep. National Renewable Energy Lab.(NREL), Golden, CO (United States)
[14] Cheung L C, Kaul C M, Hsieh A S, Blaylock M L and Churchfield M J 2020 Large-eddy simulations of the northeastern us coastal marine boundary layer *Journal of Physics: Conference Series* vol 1618 (IOP Publishing) p 062038
[15] Churchfield M J, Lee S, Michalakes J and Moriarty P J 2012 *Journal of Turbulence* **13** 1–32
[16] Moeng C H 1984 *Journal of the Atmospheric Sciences* **41** 2052–2062
[17] Beare R J, Macvean M K, Holtslag A A, Cuxart J, Esau I, Golaz J C, Jimenez M A, Khairoutdinov M, Kosovic B, Lewellen D *et al.* 2006 *Boundary-Layer Meteorology* **118** 247–272
[18] Debnath M, Doubrawa P, Optis M, Hawbecker P and Bodini N 2021 *Wind Energy Science* **6** 1043–1059 ISSN 2366-7443
[19] Optis M, Bodini N, Debnath M and Doubrawa P 2021 *Wind Energy Science* **6** 935–948 ISSN 2366-7443
[20] Banta R M, Pichugina Y L and Brewer W A 2006 *Journal of the Atmospheric Sciences* **63** 2700–2719 ISSN 0022-4928, 1520-0469